Poly(A)-specific ribonuclease deficiency impacts telomere biology and causes dyskeratosis congenita

Hemanth Tummala,[1] Amanda Walne,[1] Laura Collopy,[1] Shirleny Cardoso,[1] Josu de la Fuente,[2] Sarah Lawson,[3] James Powell,[4] Nicola Cooper,[5] Alison Foster,[5] Shehla Mohammed,[6] Vincent Plagnol,[7] Thomas Vulliamy,[1] and Inderjeet Dokal[1]

[1]Centre for Paediatrics, Barts and The London School of Medicine and Dentistry, Queen Mary University of London, Barts and The London Children's Hospital, London, United Kingdom. [2]Department of Paediatric Haematology, Imperial College Healthcare NHS Trust, St Mary's Hospital, London, United Kingdom. [3]Department of Haematology and [4]Department of Dermatology, Birmingham Children's Hospital, Birmingham, United Kingdom. [5]Clinical Genetics Unit, Birmingham Women's NHS Foundation Trust, Birmingham, United Kingdom. [6]Clinical Genetics, Guy's Hospital, London, United Kingdom. [7]University College London Genetics Institute, London, United Kingdom.

Dyskeratosis congenita (DC) and related syndromes are inherited, life-threatening bone marrow (BM) failure disorders, and approximately 40% of cases are currently uncharacterized at the genetic level. Here, using whole exome sequencing (WES), we have identified biallelic mutations in the gene encoding poly(A)-specific ribonuclease (PARN) in 3 families with individuals exhibiting severe DC. PARN is an extensively characterized exonuclease with deadenylation activity that controls mRNA stability in part and therefore regulates expression of a large number of genes. The DC-associated mutations identified affect key domains within the protein, and evaluation of patient cells revealed reduced deadenylation activity. This deadenylation deficiency caused an early DNA damage response in terms of nuclear p53 regulation, cell-cycle arrest, and reduced cell viability upon UV treatment. Individuals with biallelic *PARN* mutations and *PARN*-depleted cells exhibited reduced RNA levels for several key genes that are associated with telomere biology, specifically *TERC*, *DKC1*, *RTEL1*, and *TERF1*. Moreover, PARN-deficient cells also possessed critically short telomeres. Collectively, these results identify a role for PARN in telomere maintenance and demonstrate that it is a disease-causing gene in a subset of patients with severe DC.

Introduction

Dyskeratosis congenita (DC) and its phenotypically severe variant Hoyeraal Hreidarsson syndrome (HHS) are inherited life-threatening bone marrow (BM) failure disorders (1). X-linked recessive (OMIM 305000), autosomal dominant (OMIM 127550), and autosomal recessive (OMIM 224230) patterns of inheritance have been recognized. The classic clinical presentation of DC includes abnormal skin pigmentation, nail dystrophy, and oral leukoplakia. Individuals with DC frequently develop BM failure and are at a high risk of developing cancer, as well as a variety of other features; virtually every system can be affected in different patients. HHS is characterized by BM failure, intrauterine growth restriction, developmental delay, cerebellar hypoplasia, and immunodeficiency (2).

Pathologically, DC and HHS are characterized by selective exhaustion of highly proliferative cells that have critically shortened telomeres and exhibit an abnormal DNA damage response (3–5). Constitutional mutations in a number of genes (*DKC1*, *TERC*, *TERT*, *NOP10*, *NHP2*, *TINF2*, *TCAB1*, *CTC1*, *RTEL1*, and *ACD*) important in telomere biology are reported in DC/HHS and account for approximately 60% of all cases (1, 6–9). Five of these genes encode components of the enzyme telomerase (*TERC*, telomerase RNA; *TERT*, telomerase reverse transcriptase; *DKC1*, DC 1; *NOP10*, nucleolar protein 10 homolog; and *NHP2*, nonhistone ribonucleoprotein 2 homolog) contributing to its catalytic function. TRF1-interacting nuclear factor 2 (*TINF2*) is a component of the shelterin complex that protects the telomeric DNA. Telomerase cajal body 1 (*TCAB1* or *WRAP53*) is important in telomerase trafficking. Conserved telomere maintenance component 1 (*CTC1*) facilitates recruitment/docking of telomerase on to the telomere. Regulator of telomere elongation helicase 1 (*RTEL1*) has a critical role in telomere replication and in dismantling the telomeric t-loop. Adrenocortical dysplasia homolog (*ACD*) encodes the shelterin component TPP1, which is involved in telomerase recruitment and processivity. In view of these genetic discoveries, DC and related disorders have come to be regarded principally as disorders of defective telomere maintenance. In turn, they have highlighted the severe consequences of telomere dysfunction in humans, including BM failure, a range of severe developmental abnormalities, cancer, and premature aging.

Approximately 40% of DC/HHS patients on the Dyskeratosis Congenita Registry, London, remain uncharacterized at the genetic level. Many of these patients are sporadic cases, but in some instances, there are 2 or more affected cases in the same family. There is also considerable heterogeneity in the spectrum of features seen in the patients, ranging from some who appear to be exclusively DC or HHS to those who have overlapping features of DC and HHS. These observations suggest that the uncharacterized cases of DC/HHS are likely to be genetically heterogeneous and may harbor constitutional mutations in several genes.

▶ Related Commentary: p. 1796

Authorship note: Hemanth Tummala and Amanda Walne contributed equally to this work. Thomas Vulliamy and Inderjeet Dokal are co-senior authors.
Conflict of interest: The authors have declared that no conflict of interest exists.
Submitted: September 24, 2014; **Accepted:** February 12, 2015.
Reference information: *J Clin Invest*. 2015;125(5):2151–2160. doi:10.1172/JCI78963.

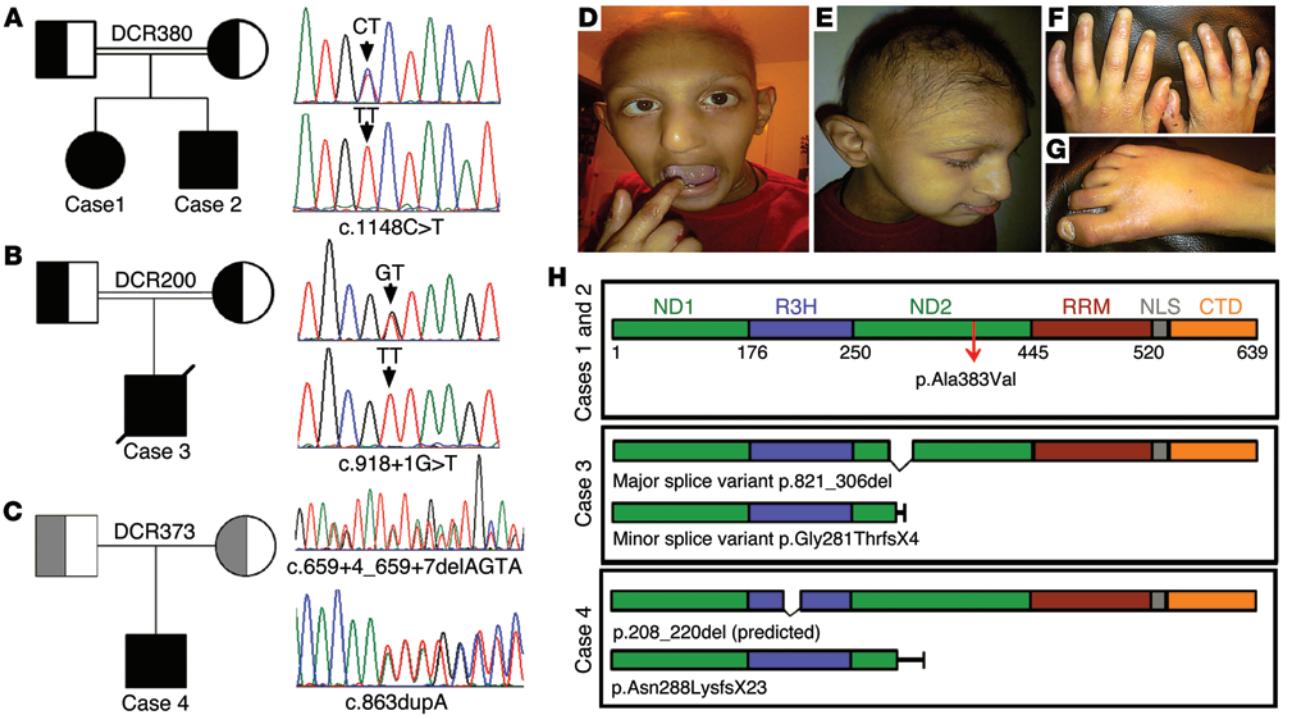

Figure 1. Identification of biallelic mutations in *PARN*. (**A**–**C**) Sanger sequencing traces confirm the presence of the mutations identified by exome sequencing in cases 1-4. Pedigrees are also shown. A representative trace of the variant is shown for parents and cases. The gray shading of the parents in DCR373 indicates that they are predicted to be heterozygous. (**D**–**G**) Photographs of case 3 showing some of the clinical features: (**D**) abnormal dentition and abnormal facial features, including dysmorphic ears and microcephaly; (**E**) sparse hair, (**F** and **G**) nail dystrophy. (**H**) A linear diagram of the PARN protein shows functional domains and the effect of mutations identified in cases 1-4 giving rise to relevant protein variants. ND1 and ND2, nuclease domain 1 and nuclease domain 2; R3H, conserved arginine and 3-histidine containing domain; RRM, RNA recognition motif; NLS, nuclear localization signal; CTD, C-terminal domain.

In this study, we employed whole exome sequence (WES) analysis to identify constitutional biallelic mutations in a new disease gene in a subgroup of patients with DC/HHS. We provide data that demonstrates that poly(A)-specific ribonuclease (PARN) deficiency due to constitutional *PARN* mutations is associated with defective telomere maintenance and causes severe DC.

Results

Identification of biallelic mutations in PARN. From our cohort of genetically uncharacterized DC families, exome sequencing was performed on a group of 31 affected individuals from 27 unrelated families that presented with either HHS or an overlap of DC/HHS. Presenting features included some or all of the following: abnormal skin pigmentation, nail dystrophy, leukoplakia, BM failure, intrauterine growth restriction, developmental delay, microcephaly, and cerebellar hypoplasia. Exome sequence data for the 31 cases were processed and called jointly with a set of 2,500 WES internal control samples (UCL-ex consortium) with unrelated medical conditions, using the recommendations from the Genome Analysis Toolkit (GATK v3.2, https://www.broadinstitute.org/gatk/) to minimize artifactual batch effects. Owing to a pattern of inheritance consistent with a recessive trait in a large proportion of cases, we focused on genes showing an excess of rare and potentially functional biallelic variants in the cases. We retained a single case per family in cases and controls so all samples could be treated as statistically independent. Using a Fisher's exact test, we then ranked all genes based on an excess of cases with at least 2 rare (allele frequency <0.5%) and functional (nonsynonymous, loss-of-function, or intronic within 5 bp of an exon-intron junction) alleles, including homozygous calls.

The top-ranked gene was *PARN*. Focusing in on PARN, we excluded related individuals and cases or controls with insufficient *PARN* coverage (<10 times the average sequencing depth across all exons). Rare (MAF <0.5%) and potentially functional biallelic variants were found in 3 of 22 unrelated cases but in none of the 1,492 UCL-ex controls; this information corresponds to a Fisher's exact test P value of 2.66×10^{-6}. To better assess the significance of this P value, we took a genomewide view and counted 5,862 genes with at least one candidate biallelic variant in the combined case-control cohort. Correcting for that number of tests using a strict Bonferroni approach yields a $P = 0.05$ corrected threshold of 8.7×10^{-5}, which our *PARN* P value of 2.66×10^{-6} exceeds. Based on this statistical evidence, we believe the biallelic variants identified in *PARN* fulfill the guidelines for implicating sequence variants in a human monogenic disease (10).

PARN variants were identified in family DCR380 (Figure 1A), as well as in 2 additional unrelated sporadic cases (DCR200 and DCR373) (Figure 1, B and C). The DCR380 case (case 1) was homozygous for the *PARN* nonsynonymous single nucleotide variant c.1148C>T and the affected individual in DCR200 (case 3) was homozygous for the potential splice-altering variant c.918+1G>T. The affected individual in DCR373 (case 4) has the

Table 1. Clinical features of cases with *PARN* mutations

Family	DCR380, case 1	DCR380, case 2	DCR270, case 3	DCR373, case 4
Sex	F	M	M	M
Age (yrs) at referral	9	6	3	10
Country of origin	Pakistan	Pakistan	Pakistan	England
Parental consanguinity	Yes	Yes	Yes	No
Learning/developmental delay	Yes	Yes[A]	Yes	Yes
Microcephaly	Yes	Yes[A]	Yes	Yes
Cerebellar hypoplasia	Yes	Yes	Yes	Yes
Mucocutaneous features				
Abnormal skin pigmentation	Yes	Yes[A]	No	Yes
Leukoplakia	Yes	Yes	Yes	No
Nail dystrophy	Yes	Yes[A]	Yes	No
Other clinical features	Yes[B]	Yes[C]	Yes[D]	Yes[E]
Trilineage BM failure	Yes[F]	Yes[G]	Yes[H]	Yes[I]
Chromosomal breakage in PB lymphocytes after treatment with DNA cross linkers	Normal	Normal	Normal	Normal

F, female; M, male. [A]More pronounced than case 1. [B]Dental caries. [C]Intrauterine growth restriction, low birth weight, failure to thrive, and sparse hair. [D]Failure to thrive, epiphora, dental and hair loss. [E]Ataxia. [F]Hemoglobin 8.4 g/dl, white cell count 2.7×10^9/l, platelets 58×10^9/l; BM hypocellular with features of dyserythropoiesis, and increase in mast cells. [G]Hemoglobin 8.9 g/dl, white cell count 3.5×10^9/l, platelets 62×10^9/l. [H]Hemoglobin 12 g/dl, white cell count 3.3×10^9/l, platelets 27×10^9/l. [I]Hemoglobin 10.4 g/dl, white cell count 4.7×10^9/l, platelets 65×10^9/l. For each of the 4 cases, the peripheral blood analysis given is at presentation, and the percentage of neutrophils and lymphocytes in the white cell count falls within the normal range (40%–80% and 20%–40%, respectively).

variants c.659+4_659+7delAGTA (potentially splice-altering) and c.863dupA (predicted frameshift loss-of-function) and is considered to be a compound heterozygote (Figure 1, A–C). All variants were confirmed in the cases and any available family members by Sanger sequencing. This additional sequencing showed that both sets of parents in DCR380 and DCR200 were heterozygous for the respective *PARN* variants, and that the DCR380-affected sibling (case 2) was homozygous for the rare allele, a pattern consistent with autosomal recessive inheritance. Parents in family DCR373 were not available for study. To our knowledge, none of these variants have been reported in any of the publicly available databases such as dbSNP (http://www.ncbi.nlm.nih.gov/SNP/), the 1000 Genomes (http://www.1000genomes.org/data), and the Exome Variant Server (http://evs.gs.washington.edu/EVS. No loss-of-function variants in *PARN* were detected in the set of 2,500 internal controls. Clinically, all cases were phenotypically similar, having tri-lineage BM failure, developmental delay, cerebellar hypoplasia, and microcephaly, as well as other features of DC/HHS (Table 1). Photographs of some of the clinical features observed in case 3 are shown in Figure 1, D–G. We screened an additional 47 DC patients from our UK registry who had a non-HHS phenotype by a combination of exome sequencing (n = 31) and targeted denaturing high-performance liquid chromatography (n = 16). This screening did not reveal additional abnormalities in *PARN*, suggesting that mutations in *PARN* are specific to the severe allelic form of DC.

Characterization of biallelic mutations in PARN. PARN belongs to a highly conserved family of exoribonucleases. It acts by shortening mRNA poly(A) tail length through the process of deadenylation and, in doing so, regulates gene expression (11–13). Structurally, PARN consists of 2 N-terminal nuclease domains (ND1 and ND2) separated by an R3H domain that consists of an invariant arginine residue followed by a highly conserved histidine residue 4 amino acids downstream. These are followed by an RNA recognition motif (RRM) domain, a nuclear localization signal (NLS), and a C-terminal domain (CTD; Figure 1H and ref. 14). The homozygous variant identified in cases 1 and 2 introduces an alanine to valine missense change at position 383 (p.Ala383Val) in the ND2 region (Figure 1H). The c.918+1G>T variant in case 3 abolishes the donor site of intron 13. RT-PCR analysis of a cDNA sample obtained from the blood of this case revealed 2 distinct bands (Supplemental Figure 1A; supplemental material available online with this article; doi:10.1172/JCI78963DS1). Sanger sequencing of the major upper band showed that exon 13 was skipped (Supplemental Figure 1B) resulting in an in-frame deletion of amino acids 281-306 (p.281_306del) in the ND2 region leading to deletion of a β sheet and an α helix in the PARN structure (Supplemental Figure 1, C, E, and F). Sequencing of the minor band revealed the loss of both exons 13 and 14; this loss would result in a frame shift, p.Gly281ThrfsX4 (Figure 1H and Supplemental Figure 1, D and G), leading to loss of the RRM and CTD domains, which are essential for RNA recognition and nuclear localization (14–16).

The 2 variants identified in case 4 are c.863dupA and c.659+4_659+7delAGTA. c.863dupA results in a frame shift and premature termination (p.Asn288LysfsX23), causing loss of the RRM domain and CTD (Figure 1H and Supplemental Figure 2, A and B). c.659+4_659+7delAGTA has an effect on the donor site of intron 9 (Figure 1H and Supplemental Figure 2C) and is predicted by the splice site analysis tool NetGene2 v2.4 (www.cbs.dtu.dk/services/NetGene2) to abolish splicing at this position (Supplemental Figure 2, D and E). We do not have cDNA available from this case, but if the preceding exon (in this case exon 9) was to be skipped, as is often observed when splice sites are disrupted, it would result in

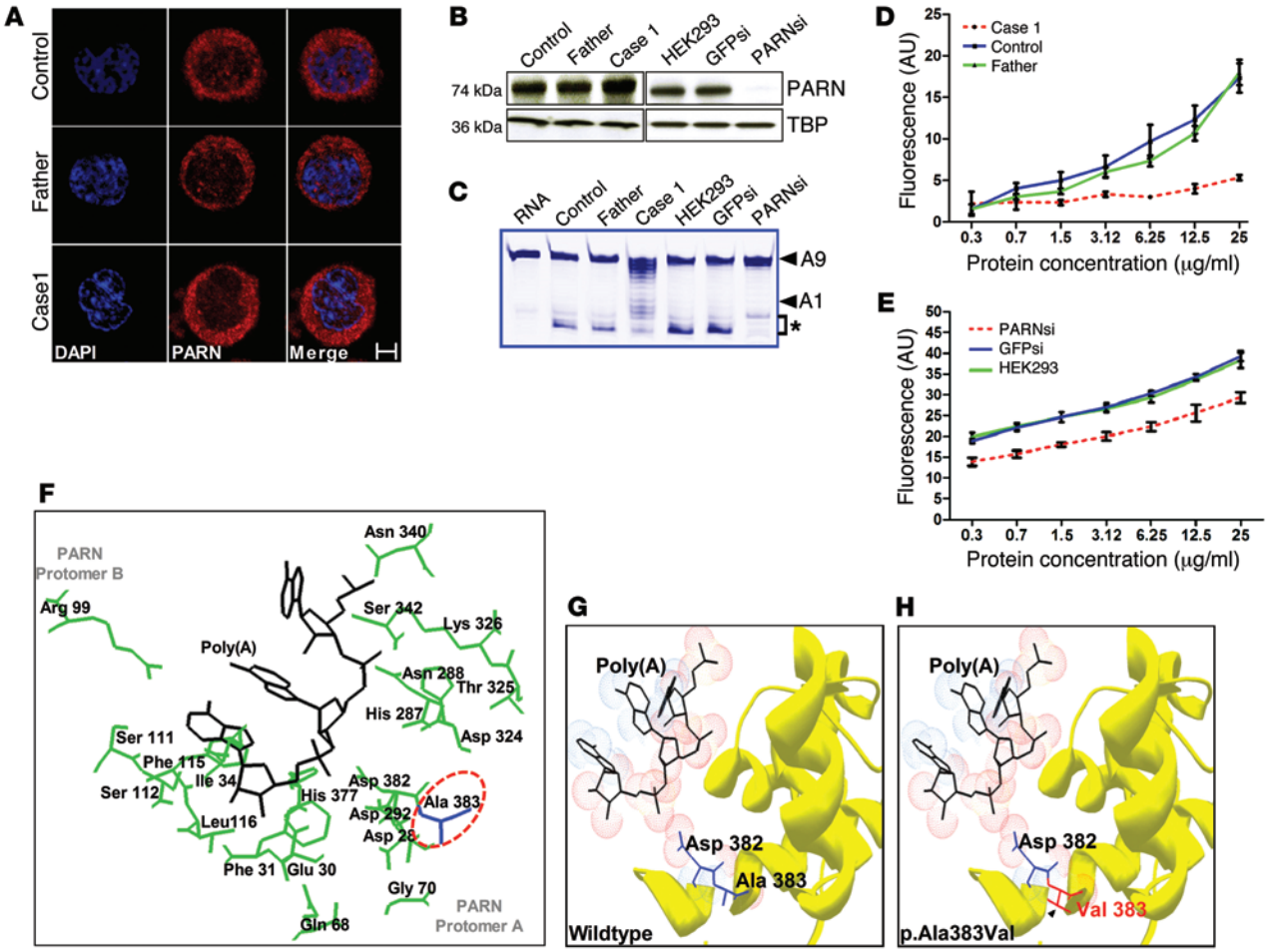

Figure 2. Mutations in *PARN* cause deadenylation deficiency. (**A** and **B**) Immunocytochemistry and Western blotting on EBV-transformed LCLs revealed no apparent differences in localization or expression of PARN between control, father, and case 1. Antibody against TATA binding protein (TBP) was used as a loading control. Immunostaining images show DAPI (blue) or PARN (red) from case 1, father, or control. Scale bar: 8 μm. (**C**) A gel-based deadenylase assay shows reduced deadenylation activity of an RNA substrate in whole-cell extracts from case 1 LCLs and PARN siRNA–treated (PARNsi-treated) HEK293 cells. The upper arrow (A9) indicates intact RNA substrates containing nine 3′ adenosine residues, the lower arrow (A1) indicates the reaction product containing a single 3′ adenosine residue, and * denotes related deadenylated products. (**D** and **E**) Fluorescence-based measurement shows reduced deadenylation kinetics in case 1 LCLs and PARNsi-treated cells. (**F**–**H**) PARN topology shows the position of p.Ala383Val missense change in the ND2 domain. (**F**) In silico analysis of PARN catalytic site (PDB 2A1R) denotes the amino acids from each promoter (ball and stick model; green) and bound RNA poly(A) (black). The mutated alanine 383 (Ala 383) residue is shown in blue. The adjacent aspartic acid 382 (Asp 382) residue has been shown to be involved in RNA poly(A) processivity (19). (**G**) Ribbon diagram (yellow) showing part of PARN nuclease domain and RNA poly(A) complex (black). (**H**) The missense change Ala 383 (blue, in **G**) to valine 383 (Val 383) (red) introduces a side chain (arrow head) in the α-helices (yellow) of PARN nuclease domain.

an in-frame deletion of amino acids 208–220 (p.208_220del) from the R3H domain of PARN (Figure 1H and Supplemental Figure 2, F and H). The R3H domain plays a prominent role in the catalytic efficiency (16) and the maintenance of structural integrity through dimerization in human PARN (15). Based on the structural alterations caused by the variants observed in cases 3 and 4, it is likely that they would have a marked effect on the function of PARN. For the missense variant p.Ala383Val identified in cases 1 and 2, we had EBV-transformed lymphoblastoid cell lines (LCLs) available in which we could directly assess the functional effect of this variant.

Cells homozygous for PARN p.Ala383Val are deadenylation-deficient. PARN localizes to both the cytosol and the nucleus, where it exerts its exonuclease activity to regulate eukaryotic mRNA transcript levels (14, 17–22). Immunostaining using a PARN-specific antibody revealed no major difference in either subcellular localization or expression levels of PARN in LCLs from case 1 expressing mutant PARN compared with LCLs from his heterozygous father and an unrelated healthy control (Figure 2A). The specificity of the antibody we used was verified in HEK293 cells treated with a PARN-specific siRNA, which revealed reduced levels of PARN when compared with untreated cells or cells treated with a GFP-control siRNA (Figure 2B).

To assess the exonuclease activity of mutant PARN, we performed an in vitro deadenylation assay on whole-cell extracts obtained from the LCLs using a fluorescent A9 RNA substrate (23). Gel-based analysis showed reduced deadenylation of the A9 substrate in case 1 when compared with his father and the unrelated control, as shown by a reduction in intensity of the deadenylated products (indicated by *) and an increase in the intensity of partially deadenylated products between A9 and A1 (Figure 2C). Due to the

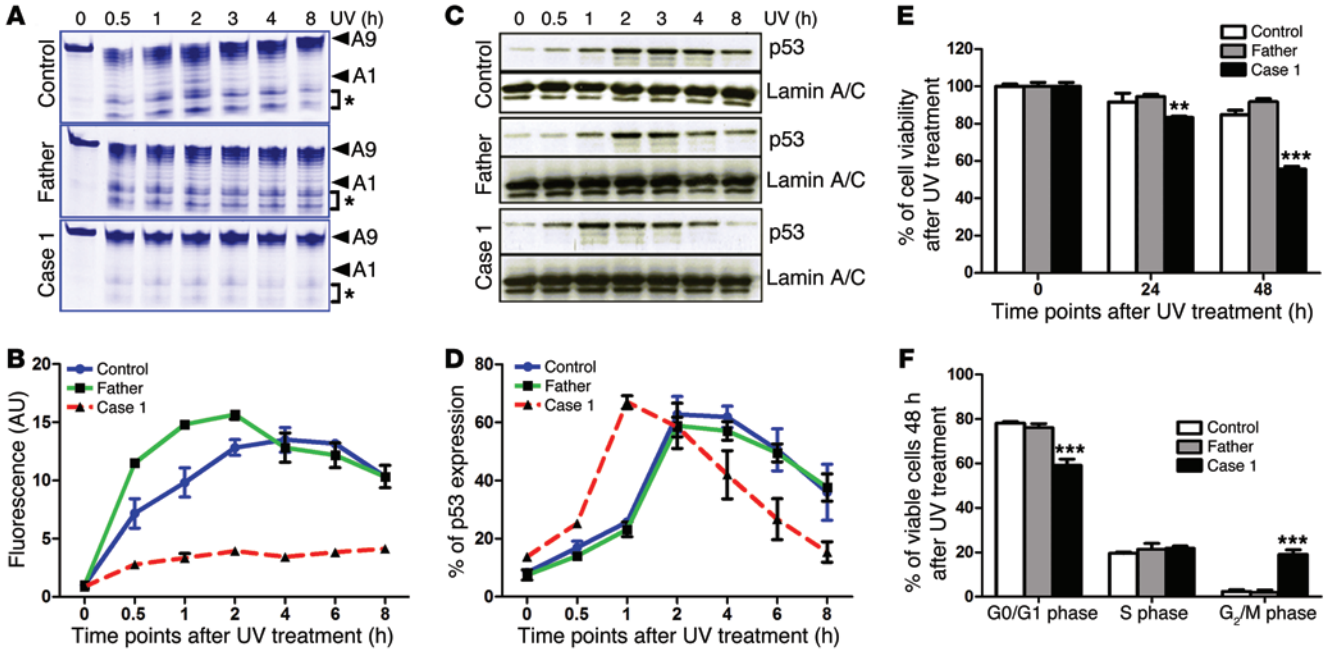

Figure 3. Lack of nuclear deadenylation and abnormal DNA damage response in PARN-deficient cells. (**A** and **B**) LCLs were exposed to UV light (40 J/m^2) and allowed to recover over the time points indicated. Nuclear extracts from these cells were then tested for deadenylase activity using a fluorescent A9 substrate in a gel-based assay. The upper arrow (A9) indicates intact RNA substrates containing nine 3′ adenosine residues, the lower arrow (A1) indicates the reaction product containing a single 3′ adenosine residue, and the * denotes related deadenylated products. (**B**) Fluorescence-based assay shows reduced deadenylation kinetics in case 1 LCL nuclear extracts upon UV stress over time when compared with father and control. (**C**) Immunoblotting using an anti-p53 antibody in case 1 LCLs compared with his father and an unrelated control. Lamin A/C is used as loading control for nuclear lysates. (**D**) Densitometric analysis of the data in **C** shows relative changes in p53 expression at the indicated time points relative to the 0-hour time point in case 1 LCLs compared with both the father and an unrelated control after exposure to UV light. (**E**) Compared with his father and an unrelated control, case 1 LCLs showed reduced survival 48 hours after UV treatment (n = 3). (**F**) Cell-cycle abnormalities in case 1 LCLs compared with his father and an unrelated control showed there is a significant increase in the proportion of viable cells in G_2/M 48 hours after treatment (n = 3). In all cases, data represent mean ± SEM, $^{**}P < 0.01$; $^{***}P < 0.0001$ 1-way ANOVA with Tukey's post hoc test.

presence of other ribonucleases in whole-cell extracts, we see deadenylated products beyond the stretch of A residues. As expected, quantitative analysis also revealed decreased deadenylase activity in case 1, in a concentration-dependent manner (Figure 2D). To ensure that the deadenylation defect observed was specifically due to defective PARN, we performed both deadenylation assays on whole-cell extracts from HEK293 cells treated with a PARN-specific siRNA. This PARN knockdown revealed reduced deadenylation of the A9 substrate compared with GFP siRNA–treated or untreated HEK cells in a concentration-dependent manner (Figure 2, C and E).

Structural studies of PARN (16, 24) have defined the amino acids that constitute the catalytic core for poly(A) binding and processivity (Protein Data Bank 2A1R; Figure 2F). Our in silico analysis of the Ala383Val substitution indicates that it would introduce a side chain in an α-helix — adjacent to the aspartic acid 382 residue — which constitutes part of the catalytic domain of PARN (Figure 2, G and H). As valine residues are known to favor β-sheet formation (25), the alanine-to-valine substitution may therefore disrupt the α-helix, causing a structural alteration in the catalytic domain. Taken together, these results indicate that the p.Ala383Val variant identified in case 1 leads to reduced PARN-specific deadenylation due to structural alterations in the PARN catalytic domain.

PARN deficiency results in an abnormal DNA damage response. Previous studies have indicated that nuclear deadenylation upon UV treatment is PARN dependent and is activated through the interaction of the CTD of PARN with cleavage stimulation factor (CstF) 50, BRCA1-associated RING domain protein (BARD1), and p53 (13, 26). The formation of this PARN/CstF/BARD1/p53 complex activates the deadenylation step to regulate mRNA transcript abundance upon DNA damage (13, 26). We were therefore interested in studying the effects of UV damage on PARN-deficient cells. We exposed case 1 and the control LCLs to UV and allowed them to recover in complete medium for varying lengths of time before nuclear extracts were prepared and assayed for deadenylation activity. This revealed reduced deadenylation of the A9 RNA substrate in case 1 when compared with his father and an unrelated control, as shown by the reduction in intensity of the bands at the bottom of the gel (indicated by asterisks) in Figure 3A and the clearly reduced fluorescence in Figure 3B.

Given this nuclear PARN deficiency after UV exposure in patient LCLs, we next investigated its effect on p53 regulation. Immunoblotting using a p53 antibody revealed an early rise in p53 levels in case 1 LCLs, which was not sustained to the same level over time when compared with the father and the control samples (Figure 3, C and D). Cell viability assay by FACS analysis 48 hours after UV treatment revealed a significant increase in cell death (Figure 3E). In addition, cell-cycle analysis revealed that a significantly increased proportion of the viable cells were arrested in

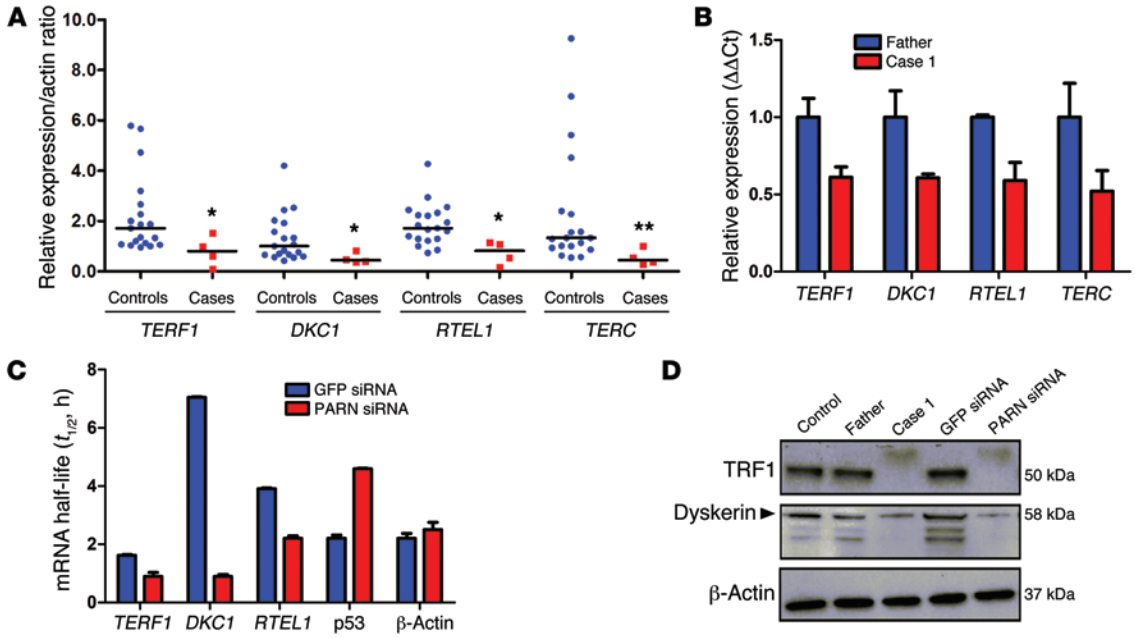

Figure 4. PARN deficiency effects telomere biology. (**A**) Cases of PARN deficiency show reduced levels of expression of 4 telomere biology genes in blood. The relative expression of each gene, after normalizing to β-actin, is shown. Samples from cases 1-3 were analyzed, (one sample each from cases 1 and 2, and two independent samples from case 3; $n = 3$ cases) and compared with controls ($n = 19$). Bars represent the median relative expression ratio (*$P < 0.05$, **$P < 0.01$ Mann-Whitney U test). (**B**) Case 1 LCLs show reduced levels of expression of 4 telomere biology genes. All genes are normalized to β-actin and are expressed relative to the father's sample. Data represent mean ± SD, $n = 3$. (**C**) Following 0, 1, 2, and 4 hours actinomycin D treatment, mRNA half-life ($t_{1/2}$) calculated as indicated in hours for each gene is determined in GFP and PARN siRNA knockdown samples. Data represent mean ± SEM, $n = 2$. (**D**) Reduced dyskerin and TRF1 protein levels in case 1 LCLs and PARN siRNA–treated cells; β-actin is used as a loading control.

the G_2/M phase in the case 1 LCLs when compared with his father and the control (Figure 3F), confirming the previous studies on the role of PARN in G_2/M checkpoint control (27). Collectively, these results demonstrate that PARN deficiency alters the p53 response following exposure to UV and results in abnormal cell-cycle regulation and impaired cell survival.

PARN deficiency effects telomere biology. To date, the role of PARN deadenylation with respect to telomere maintenance has not been investigated. Accelerated telomere shortening and consequent impairment of cell proliferation and increased levels of p53 are thought to be the molecular basis of DC pathology (4, 5, 28). It has also been demonstrated that mouse embryonic fibroblasts with increased p53 activity downregulate the expression of several genes involved in telomere biology (29) and that depletion of PARN causes an increase in p53 expression (26). These observations led us to investigate the role of PARN in telomere biology.

A preliminary study by quantitative RT-PCR amplification of 10 genes involved in telomere maintenance, of which 7 are mutated in DC, was performed using cDNA samples from the blood of cases 1 and 2, two independent blood samples from case 3, and 7 healthy control subjects. Expression levels of these mRNA transcripts (*DKC1*, *NOP10*, *NHP2*, *TERF1*, *TINF2*, *CTC1*, *OBFC1*, *TEN1*, and *RTEL1*), as well as *TERC*, were normalized to actin, and the differences between cases and controls were assessed by applying a Mann-Whitney U test. Significant differences were observed for the *DKC1*, *TERF1*, and *RTEL1* transcripts, as well as the *TERC* small nucleolar RNA (snoRNA) (Supplemental Figure 3), in the cases with biallelic *PARN* mutations compared with controls. Analysis of these 4 genes was then repeated, using the same cases but a larger group of controls ($n = 19$). The expression of these genes remained significantly decreased when compared with controls (Figure 4A). Case 1 LCLs also displayed reduced transcript levels of these 4 genes when compared with his father (Figure 4B).

We have also monitored mRNA stability following actinomycin D treatment. This revealed a significant decrease in half-life ($t_{1/2}$) of *TERF1*, *DKC1*, and *RTEL1* transcripts in the PARN knockdown cells when compared with GFP siRNA–treated cells (Figure 4C and Supplemental Figure 4). We also found that p53 mRNA was stabilized in PARN knockdown cells, while actin mRNA was unaffected; these results are in good agreement with the results previously reported (14, 26). Furthermore, immunoblotting studies confirmed a stark reduction in both TRF1 and dyskerin levels in case 1 LCLs and in PARN knockdown cells, when compared with control cells (Figure 4D). These data demonstrate that PARN deficiency effects telomere maintenance.

It is well known that individuals with DC or HHS due to constitutional mutations in *DKC1*, *TERC*, or *RTEL1* have short telomeres (6, 7). In light of this, and the reduced levels of telomere-associated genes observed in our cases, we measured telomere lengths in our PARN-deficient cases. Short telomeres at or below the first percentile were observed in cases 1 and 2 as measured by flow-FISH (Figure 5A); a similar result was obtained when telomere lengths in cases 1–3 were measured by monochrome multiplex PCR (MMqPCR) and compared with normal unrelated controls ($n = 42$, $P < 0.001$ Mann-Whitney U, Figure 5B). Telomere lengths for case 4 were not determined, as the DNA available was not of sufficient quality.

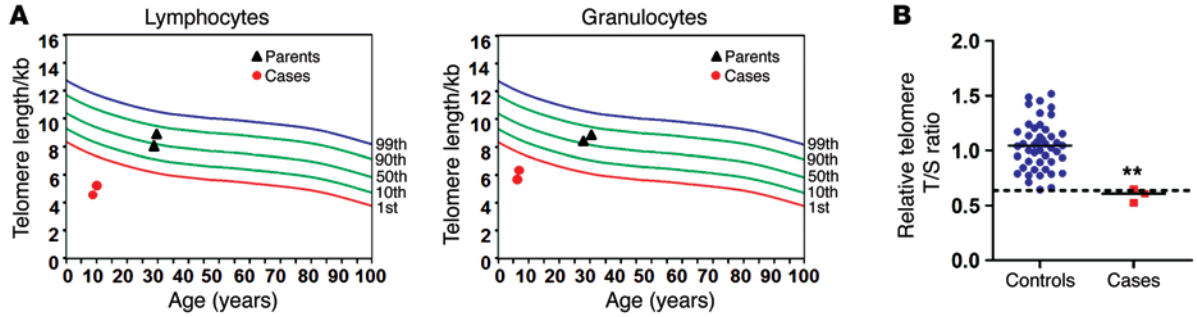

Figure 5. Telomere lengths of cases harboring *PARN* mutations. (**A**) Telomere lengths in family 1 were measured by automated multicolor flow-FISH and depicted as percentiles by calculating a reference range for telomere length over age in lymphocytes from 400 healthy individuals. Both of the affected children (indicated by red circles) show markedly shortened telomere lengths below first percentile for age in both lymphocyte and granulocyte lineages, while the parents (depicted by black triangles) have telomere lengths in the normal range. (**B**) Relative telomere lengths of cases 1–3 are reduced compared with controls. Cases 1–3 were analyzed by the MMqPCR method and compared with controls (n = 46). The dotted line represents the first percentile. Blue circles represent controls. Red squares represent cases. $^{**}P < 0.01$, Mann-Whitney U test.

Discussion

PARN is an exoribonuclease involved in the control of mRNA stability. Specifically, it is responsible for the deadenylation of poly(A) tails that is often the first step in the decay of eukaryotic mRNAs (11, 24). As a result, PARN is important in the regulation of a large number of genes/transcripts and therefore has an effect on several key cellular processes, such as cell growth, differentiation, and the DNA damage response. In this report, we show that biallelic mutations in *PARN* cause a severe DC phenotype in 4 cases from 3 unrelated families. In 2 of the families, we have identified variants that result in frameshift or splicing abnormalities. In the third family, we identified a homozygous missense variant (p.Ala383Val) affecting an amino acid that is highly conserved across species (Supplemental Figure 5) and that we showed to be catalytically defective. In this case, we found that patient cells exhibit an early DNA damage response, G_2/M arrest, and increased cell death compared with control cells. Remarkably, we have also found that PARN deficiency is associated with the downregulation of key telomere biology genes (*TERC*, *DKC1*, *RTEL1*, and *TERF1*) and critically short telomeres. However, the *TERC* reduction observed in patient cells could be a consequence of the low dyskerin levels, as previously noted (30).

Until now, there has been no clear evidence linking the function of PARN to telomere maintenance in mammalian cells, and the association may be direct or indirect. However, there are several possible connections. For example, PARN is known to be involved in nonsense-mediated mRNA decay (NMD), interacting with the key regulator of nonsense transcripts, UPF1 (31). In both yeast and human cells, it has been shown that loss of the NMD pathway upon UPF1 deletion specifically causes defects at the telomeres (32, 33). Depletion of the NMD pathway has also been shown to play a major role in hematopoietic stem and progenitor cell survival (34).

It is also possible that the effect of PARN deficiency on telomere maintenance is acting via p53. Vertebrate models of DC (29, 35, 36) and studies in human DC (4, 5, 28) have reported increased levels of p53 both in the steady state and upon DNA damage. It is also known that p53 activity regulates hematopoietic stem cell quiescence and self-renewal (37). Here, we have observed an abnormal p53 response to UV exposure in PARN-deficient patient lymphoblasts. Elsewhere, PARN knockdown in HeLa cells showed that genes involved in the p53 signalling pathway were most significantly affected (24). However, in mouse myoblasts, Lee et al. (38) reported no changes in the p53 signalling pathway upon PARN knockdown but did observe reduced abundance of telomere maintenance genes, including *Terf1*, *Terf2*, and *Rtel1*. These observations from independent studies, including our own, suggest that PARN deficiency has an effect on p53 and telomere biology, but in a cell-specific manner. Irrespective of the precise mechanism, it is clear that patients with PARN deficiency have reduced expression of several telomere biology genes and have short telomeres.

In conclusion, our results demonstrate that biallelic mutations in *PARN* are disease-causing in a subset of patients with severe DC. To our knowledge, this is the first time that the highly conserved deadenylation pathway has been shown to be involved in a human Mendelian disease.

Methods

Case selection. Exome capture was performed on a series of genetically uncharacterized cases presenting with HHS or DC/HHS overlap (n = 31 cases from 27 families) and in the DC Registry (held at Barts and The London Hospital). Presenting features included some or all of the classic mucocutaneous abnormalities (abnormal skin pigmentation, nail dystrophy, and leukoplakia) and BM failure, or at least 3 of the most commonly recognized HHS-associated features, such as intrauterine growth restriction, developmental delay, microcephaly, and cerebellar hypoplasia.

Exome capture and variant profiling. Genomic DNA, after passing quality control, was subjected to library preparation and exon capture using the TruSeq Exome Enrichment Kit (Illumina). Using the Illumina HighSeq 2000 system, 100 bp paired end reads were generated. Sequencing data were processed through the Illumina pipeline. Raw FASTQ files were aligned to the GRCh37 reference genome using Novoalign version 2.08.03 (Novocraft Technologies). Duplicate reads were marked using Picard tools MarkDuplicates. Calling was performed using the haplotype caller module of GATK (https://www.broadinstitute.org/gatk, version 3.1-1), creating gVCF-formatted files for each sample. The individual patient gVCF files, in combination with 2,500 clinical exomes (UCL-exomes consortium), were combined into

merged VCF files for each chromosome containing, on average, 100 samples each. The final variant calling was performed using the GATK Genotype GVCFs module jointly for all samples (cases and controls). Variant quality scores were then recalibrated according to GATK best practices separately for indels and SNPs. Resulting variants were annotated using ANNOVAR based on ensembl data. Candidate variants were filtered based on function (nonsynonymous, presumed loss-of-function, or splicing) and minor allele frequency (<0.5% minor allele frequency in our internal control group, as well as the NHLBI exome sequencing dataset). Splice variants were flagged within 5 bp of the exon-intron junction. All relevant variants identified were validated by Sanger sequencing on a 3130xl Genetic Analyzer with a BigDye Terminator v3.1 Cycle Sequencing Kit (Applied Biosystems). The findings of the WES studies have been deposited in the ClinVar archive at the NCBI under the accession numbers SCV000206797, SCV000206798, and SCV000206799 (http://www.ncbi.nlm.nih.gov/clinvar/).

Screening for mutation by denaturing HPLC. All exons and flanking intronic sequences of *PARN* were amplified using standard PCRs (primer sequences available on request), mixed pairwise, and scanned for mutation by denaturing high-performance liquid chromatography on a Wave DNA fragment analysis system (Transgenomic). Any fragments showing abnormal elution patterns were reamplified, and the variant was confirmed by forward and reverse Sanger sequencing.

Cell culture and treatments. EBV-infected LCLs were established and grown in RPMI Media 1640 supplemented with penicillin and streptomycin, 2 mM L-glutamine, and 20% (vol/vol) FBS (Invitrogen). HEK293 cells (ATCC CRL-1573) were cultured in DMEM supplemented with penicillin and streptomycin, 2 mM L-glutamine (FBS; 10%). For siRNA studies, HEK293 cells were seeded in T25 flasks in antibiotic-free DMEM containing 10% FBS and were transfected the following day using Lipofectamine RNAiMAX (Invitrogen). GFP siRNA (EHUEGFP) was used as a negative control, and 300 pmol of a pool of siRNAs (EHU015391) was used for PARN knockdown (Sigma-Aldrich). LCL cultures (~3×10^6 cells) were exposed to UV and harvested at the indicated time points. UV doses (40 J/m^2) were delivered in 2 pulses using a Stratalinker (Stratagene). Before UV pulsing, the medium was removed and replaced immediately after treatment.

Protein extraction and immunoblotting. For whole-cell extracts, briefly, 3×10^6 LCLs were pelleted and lysed in 3 volumes of lysis buffer (1 M HEPES, 2 M NaCl, 0.5 M NaF, 1 M Na_3VO_4, 0.5 M EDTA, 0.1% NP40, and 1× cocktail of protease inhibitors; Roche Diagnostics). Nuclear extracts from LCLs were prepared as described previously (39), both at steady state and after UV treatment at indicated time points. Briefly, LCLs were pelleted and dounced in 0.4 ml of 10 mM Tris pH 7.9, 1.5 mM $MgCl_2$, 10 mM KCl, 0.5 mM dithiothreitol (DTT), and 0.5 mM phenylmethylsulfonyl fluoride (PMSF). Dounced lysates were then centrifuged for 10 minutes at 6,000 *g*, and pellets were resuspended in 20 mM Tris pH 7.9, 1.5 mM $MgCl_2$, 25% glycerol, 0.2 mM EDTA, 0.5 mM DTT, 0.5 mM PMSF, and 0.3 M NaCl. Pellet preparations were rocked for 2 hours at 4°C and centrifuged at 8,000 *g*. Supernatants were quick-frozen and stored at –80°C. BSA-quantified nuclear extracts (30 μg) from LCLs were loaded on 4%–12% (wt/vol) Tris Glycine Gels (Invitrogen)and electroblotted onto polyvinyl difluoride (PVDF) membrane and probed with the following primary antibodies: mouse p53(DO-1) antibody (catalog SC126; Santa Cruz Biotechnology Inc.), mouse PARN antibody (catalog Ab89831; Abcam), mouse TRF1 antibody (catalog ab10579; Abcam), and rabbit dyskerin antibody (catalog ab64667; Abcam). Rabbit anti-Lamin A/B (catalog SC20681; Santa Cruz Biotechnology Inc.), rabbit polyclonal to the TATA binding protein (TBP; catalog Ab125009; Abcam), and rabbit polyclonal to β-actin (catalog Ab8227; Abcam) were used as loading controls.

Deadenylation assays. Deadenylation studies were performed as described previously (23). Briefly, in a final volume of 10 μl, 1 μM of 16-mer RNA substrate oligonucleotide (5′-CCUUUC CAAAAAAAAA-3′) containing a 5′ fluorescein (Flc) group (Sigma-Aldrich) was incubated with BSA-quantified whole-cell extracts and nuclear extracts at the indicated concentration in deadenylation buffer (20 mM Tris–HCl pH 7.9, 50 mM NaCl, 2 mM $MgCl_2$, 10% glycerol, 1 mM β-mercaptoethanol) for 1 hour at 30°C. For gel-based analysis, 3 μl of reaction was stopped by the addition of 12 μl RNA loading buffer consisting of 95% formamide, 0.025% bromophenol blue, 0.025% xylene cyanol FF, 0.025% sodium dodecyl sulphate, and 5 mM ethylene diamine tetra acetic acid (EDTA). The samples were heated for 3 minutes at 85°C and analyzed by denaturing PAGE using a 20% acrylamide:bisacrylamide (19:1) gel containing 50% (w/v) urea. Polyacrylamide gels (Bio-Rad) were prerun for 30 minutes at 200 V before sample loading. Flc-labelled RNA was visualized using a Typhoon image scanner at 460 nm (GE Healthcare). For quantitative analysis of deadenylase activity, the rest of the reaction volume (7 μl) was mixed with 5 μM DNA probe mix (5′-TTTTTTTTTG-GAAAGG-3′) containing a 3′ tetra methyl rhodamine in 1% SDS. Fluorescence intensity was measured using a BioTek Synergy HT plate reader at 485 ± 20 nm (excitation) and 528 ± 20 nm (emission).

Immunofluorescence and microscopy. LCLs were washed in warm PBS, spread on polylysine-coated slides, and fixed in 4% paraformaldehyde. After fixation, cells were permeabilized with 0.1% Triton X-100 (TX100) (Sigma-Aldrich) in PBS, quenched in 50 mM NH_4Cl, and blocked in 10% goat serum and 1% BSA in PBS containing 0.05% TX100 for 1 hour. Cells were incubated in the primary PARN antibody (Abcam) and the corresponding goat antimouse secondary antibody conjugated to Alexa Fluor 568 (Invitrogen) in blocking solution for 1 hour sequentially. Cells were washed 3 times in PBS containing 0.05% TX100 between primary and secondary antibody incubations, and mounted with vectashield containing DAPI (Vector Laboratories). Images were collected with an LSM710 laser scanning confocal microscope (Zeiss) under relevant laser excitation, and the emitted signals were visualized with ZEN software (Zeiss).

Cell cycle and cell viability analysis. Forty-eight hours after exposure to UV light (40 J/m^2), ~3×10^6 LCL cells were washed in PBS; propidium iodide (PI) was added to the cell suspension to a final concentration of 5 μg/ml, and the cells were analyzed on an LSRII Flow Cytometer (BD Biosciences). G0/G1, S and G_2/M populations were determined using standard methods. Cells (0.2×10^6) were fixed overnight in 70% ethanol, washed twice in PBS, and resuspended in 300 μl PBS with PI (50 μg/ml) and ribonuclease A (RNase A) (200 μg/ml). Cells were incubated at 37°C for 30 minutes before being analyzed on the flow cytometer. Cells were pulse-width gated to exclude doublets.

RT-PCR for mRNA abundance and stability assays. Total RNA was purified from peripheral blood using the RNeasy kit (QIAGEN) or was extracted from cells treated with siRNA using TRIzol Reagent (Invitrogen). Equivalent amounts (300 ng) of purified RNA were used as a template to synthesize cDNA using random hexamers and Superscript III reverse transcriptase (Invitrogen) according to the manufacturer's protocol. qPCR reactions were performed using SYBR Select Master Mix (Applied Biosystems) and 0.3 mM of each primer (obtained from

Sigma-Aldrich, Supplemental Table 1) and run on an ABI 7500 real-time PCR machine (Applied Biosystems). Reactions were set up in duplicate, and the relative gene expression level was calculated. Data was expressed by normalizing to β-actin (a non-PARN target gene that is not affected by PARN exonuclease activity) (13, 26). This ratio was normalized to a reference sample that was run on each plate. Relative gene expression from the LCLs was calculated using the ΔΔCt method on triplicate reads from 3 independent cDNA preparations of each cell line.

For the mRNA stability assays, in order to suppress transcription, cells were treated with actinomycin D (5 μg/ml final concentration, Sigma-Aldrich) 48 hours after transfection with either PARN or GFP siRNAs. At 0, 1, 2, and 4 hours after the addition of actinomycin D, cells were harvested, total RNA was extracted, and cDNA was synthesized using oligo dT (20-mer) as described above (Life Technologies). qPCR reactions were set up in triplicate from 2 independent experiments. Ct data were quantified against a standard curve before being normalized to their own siRNA treatment t = 0 value. One-phase exponential decay curve analysis was used to assess the mRNA half-lives.

Telomere length measurement. Telomere lengths were measured using an MMqPCR method, adapted for use on a LightCycler 480 real-time thermocycler (Roche Life Science) as described previously (40). Briefly, in each well, amplification of telomeric DNA (T) and a single copy gene (S) were quantified against standard curves obtained from dilution of a reference DNA sample. The T/S ratio, obtained in triplicate for each sample, is proportional to the telomere length. This ratio was normalized to the T/S ratio of a second reference sample that was run on every plate to give a relative T/S ratio. Automated multicolor flow-FISH analysis (41) has also been performed on blood sample subsets obtained from family 1 by Repeat Diagnostics.

Structural analysis of the PARN variants. The ternary complex of PARN crystal structures (PBD 2A1R and 2A1S) are obtained from PBD (http://www.rcsb.org) and visualized using Swiss-PDB viewer (http://spdbv.vital-it.ch/) (42). The predicted effects of missense, deletions, and truncations — resulting from the PARN mutations — were generated using this program.

Statistics. Analyses were performed with GraphPad Prism 5.0 software (GraphPad Software). Mann-Whitney U test, 1-way ANOVA with Tukey's post hoc tests, and 1-phase exponential decay–curve analyses were used when appropriate as indicated within the text or figure legends. Data are presented as the means ± SEM unless otherwise indicated. A 2-tailed P value of <0.05 was considered significant.

Study approval. All experiments were conducted with the approval of Barts and The London Hospital. Peripheral blood samples were obtained with written consent under the approval of our local research ethics committee (London – City and East). All clinical photographs appear with parental informed written consent.

Acknowledgments

We would like to thank the families and clinicians who contributed to this research, especially Heinz Jungbluth. This work was funded by The Medical Research Council UK (MR/K000292/1) and Children with Cancer UK (2013/144). All work in this study was conducted with informed, written consent and approval of the local ethics committee. Authors would like to thank Gary Warnes for support in FACS and staff at the Barts and the London Genome Centre for Sanger sequencing analysis.

Address correspondence to: Thomas Vulliamy, Centre for Paediatrics, Blizard Institute, Barts and The London School of Medicine and Dentistry, Queen Mary University of London, 4 Newark St, London, E1 2AT, United Kingdom. Phone: 44.207.882.2623; E-mail: t.vulliamy@qmul.ac.uk.

1. Dokal I. Dyskeratosis congenita. *Hematology Am Soc Hematol Educ Program*. 2011;2011:480–486.
2. Knight SW, et al. Unexplained aplastic anaemia, immunodeficiency, and cerebellar hypoplasia (Hoyeraal-Hreidarsson syndrome) due to mutations in the dyskeratosis congenita gene, DKC1. *Br J Haematol*. 1999;107(2):335–339.
3. Gu B, Bessler M, Mason PJ. Dyskerin, telomerase and the DNA damage response. *Cell Cycle*. 2009;8(1):6–10.
4. Kirwan M, et al. Dyskeratosis congenita and the DNA damage response. *Br J Haematol*. 2011;153(5):634–643.
5. Pereboeva L, et al. DNA damage responses and oxidative stress in dyskeratosis congenita. *PLoS One*. 2013;8(10):e76473.
6. Gramatges MM, Bertuch AA. Short telomeres: from dyskeratosis congenita to sporadic aplastic anemia and malignancy. *Transl Res*. 2013;162(6):353–363.
7. Savage SA. Human telomeres and telomere biology disorders. *Prog Mol Biol Transl Sci*. 2014;125:41–66.
8. Guo Y, et al. Inherited bone marrow failure associated with germ line mutation of ACD, the gene encoding telomere protein TPP1. *Blood*. 2014;124(18):2767–2774.
9. Kocak H, et al. Hoyeraal-Hreidarsson syndrome caused by a germ line mutation in the TEL patch of the telomere protein TPP1. *Genes Dev*. 2014;28(19):2090–2102.
10. MacArthur DG, et al. Guidelines for investigating causality of sequence variants in human disease. *Nature*. 2014;508(7497):469–476.
11. Mitchell P, Tollervey D. mRNA stability in eukaryotes. *Curr Opin Genet Dev*. 2000;10(2):193–198.
12. Parker R, Song H. The enzymes and control of eukaryotic mRNA turnover. *Nat Struct Mol Biol*. 2004;11(2):121–127.
13. Cevher MA, et al. Nuclear deadenylation/polyadenylation factors regulate 3′ processing in response to DNA damage. *EMBO J*. 2010;29(10):1674–1687.
14. Korner CG, Wahle E. Poly(A) tail shortening by a mammalian poly(A)-specific 3′-exoribonuclease. *J Biol Chem*. 1997;272(16):10448–10456.
15. He GJ, Zhang A, Liu WF, Yan YB. Distinct roles of the R3H and RRM domains in poly(A)-specific ribonuclease structural integrity and catalysis. *Biochim Biophys Acta*. 2013;1834(6):1089–1098.
16. Wu M, Reuter M, Lilie H, Liu Y, Wahle E, Song H. Structural insight into poly(A) binding and catalytic mechanism of human PARN. *EMBO J*. 2005;24(23):4082–4093.
17. Korner CG, Wormington M, Muckenthalar M, Schneider S, Dehlin E, Wahle E. The deadenylating nuclease (DAN) is involved in poly(A) tail removal during trhe meiotic maturation of Xenopus oocytes. *EMBO J*. 1998;17(18):5427–5437.
18. Dehlin E, Wormington M, Korner CG, Wahle E. Cap-deadenylation of mRNA. *EMBO J*. 2000;19(5):1079–1086.
19. Gao M, Fritz DT, Ford LP, Wilusz J. Interaction between a poly(A)-specific ribonuclease and the 5′ cap influenzes mRNA deadenylation rates in vitro. *Mol Cell*. 2000;5(3):478–488.
20. Martinez J, Ren YG, Nilsson P, Ehrenberg M, Virtanen A. The mRNA cap structure stimulates rate of poly(A) removal and amplifies processivity of degradation. *J Biol Chem*. 2001;276(30):27923–27929.
21. Nilsson P, et al. A multifunctional RNA recognition motif in poly(A)-specific ribonuclease with cap and poly(A) binding properties. *J Biol Chem*. 2007;282(45):32902–32910.
22. Wu M, et al. Structural basis of m(7)GpppG binding to poly(A)-specific ribonuclease. *Structure*. 2009;17(2):276–286.
23. Maryati M, et al. A fluorescence-based assay suitable for quantitative analysis odeadenylase enzyme activity. *Nucleic Acids Res*. 2014;42(5):e30.
24. Vlachakis D, et al. An integrated in silico approach to design specific inhibitors targeting human poly(A)-specific ribonuclease. *PLoS One*. 2012;7(12):e51113.
25. Zhu BY, Zhou NE, Kay CM, Hodges RS. Packing

and hydrophobicity effects on protein folding and stability: effects of β-branched amino acids, valine and isoleucine, on the formation and stability of two-stranded α-helical coiled coils/leucine zippers. *Protein Sci*. 1993;2(3):383–394.
26. Devany E, Zhang X, Park JY, Tian B, Kleiman FE. Positive and negative feedback loops in the p53 and mRNA 3′ processing pathways. *Proc Natl Acad Sci U S A*. 2013;110(9):3351–3356.
27. Reinhardt HC, et al. DNA damage activates a spatially distinct late cytoplasmic cell-cycle checkpoint network controlled by MK2-mediated RNA stabilization. *Mol Cell*. 2010;40(1):34–49.
28. Carrillo J, González A, Manguán-García C, Pintado-Berninches L, Perona R. p53 pathway activation by telomere attrition in X-DC primary fibroblasts occurs in the absence of ribosome biogenesis failure and as a consequence of DNA damage. *Clin Transl Oncol*. 2014;16(6):529–538.
29. Simeonova I, et al. Mutant mice lacking the p53 C-terminal domain model telomere syndromes. *Cell Rep*. 2013;3(6):2046–2058.
30. Mitchell JR, Wood E, Collins K. A telomerase component is defective in the human disease dyskeratosis congenita. *Nature*. 1999;402(6761):551–555.
31. Lejeune F, Li X, Maquat LE. Nonsense-mediated mRNA decay in mammalian cells involves decapping, deadenylating, and exonucleolytic activities. *Mol Cell*. 2003;12(3):675–687.
32. Lew JE, Enomoto S, Berman J. Telomere length regulation and telomeric chromatin require the nonsense-mediated mRNA decay pathway. *Mol Cell Biol*. 1998;18(10):6121–6130.
33. Azzalin CM, Reichenbach P, Khoriauli L, Giulotto E, Lingner J. Telomeric repeat containing RNA and RNA surveillance factors at mammalian chromosome ends. *Science*. 2007;318(5851):798–801.
34. Weischenfeldt J, et al. NMD is essential for hematopoietic stem and progenitor cells and for eliminating by-products of programmed DNA rearrangements. *Genes Dev*. 2008;22(10):1381–1396.
35. Zhang Y, Morimoto K, Danilova N, Zhang B, Lin S. Zebrafish models for dyskeratosis congenita reveal critical roles of p53 activation contributing to hematopoietic defects through RNA processing. *PLoS One*. 2012;7(1):e30188.
36. Pereboom TC, van Weele LJ, Bondt A, MacInnes AW. A zebrafish model of Dyskeratosis congenita reveals hematopoietic stem cell formation failure resulting from ribosomal protein-mediated p53 stabilization. *Blood*. 2011;118(20):5458–5464.
37. Pant V, Quintás-Cardama A, Lozano G. The p53 pathway in hematopoiesis: lessons from mouse models, implications for humans. *Blood*. 2012;120(26):5118–5127.
38. Lee JE, Lee JY, Trembly J, Wilusz J, Tian B, Wilusz CJ. The PARN deadenylase targets a discrete set of mRNAs for decay and regulates cell motility in mouse myoblasts. *PLoS Genet*. 2012;8(8):e1002901.
39. Kleiman FE, Manley JL. The BARD1-CstF-50 interaction links mRNA 3′ end formation to DNA damage and tumor suppression. *Cell*. 2001;104(5):743–753.
40. Cawthon RM. Telomere length measurement by a novel monochrome multiplex quantitation PCR method. *Nucleic Acids Res*. 2009;37(3):e21.
41. Baerlocher GM, Vulto I, de Jong G, Lansdorp PM. Flow cytometry and FISH to measure the average length of telomeres (flow FISH). *Nat Protoc*. 2006;1(5):2365–2376.
42. Guex N, Peitsch MC. SWISS-MODEL and the Swiss-PdbViewer: an environment for comparative protein modeling. *Electrophoresis*. 1997;18(15):2714–2723.